## PAPER

Check for updates

# Substitution-induced changes in the structure, vibrational, and magnetic properties of BiFeO₃

I. Kallel,[a] Z. Abdelkafi, ID *[a] N. Abdelmoula,[a] H. Khemakhem,[a]
N. Randrianantoandro[b] and E. K. Hlil[c]

To address practical progress and prospective applications of BiFeO₃, particularly in the development of data storage devices, we substituted it with the perovskite $BaTi_{0.9}Zr_{0.1}O_3$ to form the system $(1 - x)BiFeO_3$-$(x)BaTi_{0.9}Zr_{0.1}O_3$, limiting $x$ to the range of 0–0.4. We prepared these compositions using the solid-state reaction method, highlighting the correlation between their structure, vibrational properties, and magnetic response. X-ray diffraction and Raman scattering spectra reveal the structural transition from the $R3c$ rhombohedral to $Pm\bar{3}m$ cubic with increasing the content of $BaTi_{0.9}Zr_{0.1}O_3$. Mössbauer spectroscopy investigation indicates that the substitution of $Fe^{3+}$ ions with $Ti^{4+}$ and $Zr^{4+}$ weakens the Dzyaloshinskii–Moriya (DM) interaction. Thus, the DM interaction becomes subordinate to the exchange interaction in the G-type antiferromagnetic order of $Fe^{3+}$ ions within the BFO structure, potentially suppressing the cycloidal spin configuration in the samples $x = 0.1$, 0.2, and 0.3. The mean hyperfine magnetic fields decreased with the increasing ($x$) of $BaTi_{0.9}Zr_{0.1}O_3$, and a paramagnetic phase was observed for $x = 0.4$. The decrease of quadrupole splitting/shift ($\Delta E_Q/2\varepsilon$) for $x = 0.1$, 0.2, and 0.3 indicates a transition toward a higher-symmetry environment around $Fe^{3+}$ due to the substitution. This result proves the structural transition from the $R3c$ rhombohedral to $Pm\bar{3}m$ cubic observed by X-ray diffraction and Raman spectroscopy as the content of $BaTi_{0.9}Zr_{0.1}O_3$ increases. Using Rietveld refinement data of X-ray diffraction, the calculation of the tilt angle ($\omega$) reveals a decrease in the level of the rhombohedral structure. For compositions exceeding $x = 0.1$, the decrease in $\omega$ with the substitution rate leads to a reduction in remanent magnetization. However, the enhancement of remanent magnetization ($M_r \sim 0.34$ emu g$^{-1}$) was observed for $x = 0.1$. Moreover, hysteresis loops for the compositions $x = 0.1$ and 0.2 exhibit smaller field coercivity at 2 K compared to 300 K, which could identify the presence of magnetoelectric coupling in this system.

## 1. Introduction

The domain of magnetoelectric multiferroics continues to attract significant interest due to the coupling of ferroelectric and magnetic order characteristics, considering the potential applications in a range of multifunctional areas such as high energy-storage performance,[1] data storage[2] and neuromorphic computing.[3] One of the most extensively researched multiferroics, bismuth ferrite BiFeO₃ (BFO), bears both magnetic and ferroelectric properties at room temperature (RT), with high Néel ($T_N \sim 630$ K) and Curie ($T_C \sim 1100$ K) temperatures.[4] It presents a significant polarization of about 100 μC cm$^{-2}$ (ref. 5)

resulting from the displacement of Fe and Bi atoms.[6] Neutron diffraction studies prove a negative magnetostriction that reduces the spontaneous polarization caused by the suppressed displacement of Fe below $T_N$.[7]

The structure of BFO was classified as rhombohedral distorted perovskite, which is affiliated with the $R3c$ space group. This structure is typified by ionic displacements from centrosymmetric position and antiphase tilt of octahedral FeO₆ ($a^-a^-a^-$ in Glazer notation), which occurs across the same direction [001].[8] Besides, the magnetic structure of BFO is G-type antiferromagnetic, with all six nearest magnetic neighbors oriented antiferromagnetically, which exhibits a superimposed spin cycloid with an incommensurate period of 62 nm.[9] As a result, weak ferromagnetism arises from the Dzyaloshinskii–Moriya interaction, which averages to zero in the bulk of BFO.[10,11] This state has a negative impact on the observation of the linear magnetoelectric effect,[10–12] hindering its potential use in devices. Several attempts have been made to suppress the cycloid by using different techniques in order to recover a nonzero macroscopic

[a] *Laboratory of Multifunctional Materials and Applications (LaMMA), LR16ES18, Faculty of Sciences of Sfax, University of Sfax, B.P. 1171, 3000 Sfax, Tunisia. E-mail: zied_abdelkafi@yahoo.fr*

[b] *Institut des Molécules et Matériaux du Mans – UMR 6283, CNRS – Le Mans Université, Avenue Olivier Messaien, Le Mans 72085, France*
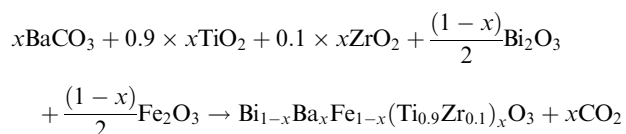
[c] *Institut Néel, Université Grenoble Alpes, CNRS, BP 166, F-38042 Grenoble cedex 9, France*

magnetization as well as the linear magnetoelectric effect.[13–18] A high magnetic field has been used to destroy the cycloidal spin structure, causing a transition from the cycloidal modulated spin structure to a homogeneous G-type antiferromagnetic structure.[17] Similarly, the thin film BFO induces the destruction of the spin cycloid due to the epitaxial strain.[18] Several efforts have been made to improve the magnetization in BFO, mostly focusing on the potential of chemical substitution to release a weak remanent magnetization of BFO, typically within the range of $M_r \sim 0.1$ to 0.3 emu g$^{-1}$.[13–16] The origin of weak magnetization in the compound $(Bi_{0.8}La_{0.2})(Fe,Ga)O_3$-43%$PbTiO_3$[13] was explained by the Landau–Ginzburg theory,[17] in which an energy perturbation is sufficient to make a transition from a cycloidal spin structure to a homogenous one. Based on this theory, Park et al.[19] have shown that the $(1 - x)BaTiO_3$-$xBiFeO_3$ solid solution nanostructures exhibit magnetoelectric characteristics, leading to a decrease in coercive field ($H_c$) at low temperatures relative to RT. In the same work, a high value of remanent magnetization ($M_r \sim 0.75$ emu g$^{-1}$) was observed for the composition $x = 0.2$. In addition, in the work of A. Singh[16] on the $(1 - x)BiFeO_3$-$xBaTiO_3$ ceramics, an evolution of remanent magnetization was observed. Notably, a significant remanent magnetization of 0.16 emu g$^{-1}$ was detected for the composition $x = 0.2$. To the best of our knowledge, there have been no previous reports on the solid solution $(1 - x)BiFeO_3$-$(x)BaTi_{0.9}Zr_{0.1}O_3$, specifically examining structural, vibrational and magnetic proprieties.

In our recent work, $BaZr_{0.1}Ti_{0.9}O_3$ substituted BFO was studied, particularly for $x = 0.1$.[20] In this study, we have shown that the coupling between hyperfine field ($H_{hf}$) and polarization ($P$) (calculated from Rietveld refined atomic) occurs via magnetoelastic coupling within the lattice. Moreover, we have demonstrated that the evolution of $H_{hf}$ as a function of $P$ below $T_N$ exhibits a linear trend, and the magnetoelectric coupling coefficient value ($\alpha_{ME}$) is around $1.84 \times 10^{-9}$ s m$^{-1}$. In this present work, we aim to extend this study by increasing the substitution rate in the $(1 - x)BiFeO_3$-$xBaZr_{0.1}Ti_{0.9}O_3$ system. Thus, the substitution rates of interest in this work are $x = 0$, $x = 0.1$, $x = 0.2$, $x = 0.3$ and $x = 0.4$. In light of earlier research, we propose a coherent mechanism to reach a comprehensive correlation between crystalline structural distortion, vibrational band, and magnetic properties within this system.

## 2. Experimental procedure

The system $(1 - x)BiFeO_3$-$(x)BaTi_{0.9}Zr_{0.1}O_3$ within the range of $0 \leq x \leq 0.4$ was synthesized via solid-state reaction. The chemical equation for the synthesis of these samples is the following:

$$xBaCO_3 + 0.9 \times xTiO_2 + 0.1 \times xZrO_2 + \frac{(1-x)}{2}Bi_2O_3$$

$$+ \frac{(1-x)}{2}Fe_2O_3 \rightarrow Bi_{1-x}Ba_xFe_{1-x}(Ti_{0.9}Zr_{0.1})_xO_3 + xCO_2$$

$BaCO_3$, $TiO_2$, $ZrO_2$, $Bi_2O_3$, and $Fe_2O_3$ were used as starting reagents. These powders were accurately weighed in stoichiometric ratios and mixed thoroughly in an agate mortar for 1 hour.

The resulting mixture was rapidly calcined at temperatures of 873 K, 973 K, and 1103 K for 1 hour in air, with intermediate grindings for 1 hour. After calcination, the powders were mixed for another hour and pressed under 100 MPa into pellets with dimensions of 8 mm in diameter and approximately 1.5 mm in thickness. These pellets were then sintered in air for 2 hours at 1223 K. A ceramic BFO sample was synthesized following the solid-state technique reported by Achenbach et al.[21] The X-ray diffraction (XRD) measurements were carried out with an EMPYREAN X-ray diffractometer using Cu-K$\alpha_{1,2}$ radiations ($\lambda_1 = 1.5406$ Å, $\lambda_2 = 1.544$ Å). Structural analyses were performed via powder XRD, using an 18 KW Cu-rotating anode. The microstructural analysis was conducted using a JEOL JSM 6510 LV scanning electron microscope (SEM) with an X-Max N20 detector. The SEM-energy dispersive spectroscopy (SEM-EDS) mapping was performed using Zeiss GeminiSEM 560 equipped with a field emission gun (FEG) and an Oxford Instruments energy-dispersive X-ray spectroscopy (EDS) detector. Raman spectra were recorded at RT in the spectral range of 50 to 700 cm$^{-1}$ in a micro-Raman spectrometer (LABRAM HR-800), working in a backscattering configuration, equipped with an Argon Ion Laser line, at 514.5 nm. $^{57}$Fe Mössbauer spectra were displayed in transmission geometry with a constant acceleration spectrometer, via a $^{57}$Co source diffused in a rhodium matrix. Isomer shift values were referenced to α-Fe. Mössbauer experiments were carried out in transmission geometry at RT. The samples were placed in a furnace under vacuum. Mössbauer data were analyzed using the MOSFIT program,[22] which permits the use of a distribution of hyperfine structures as components of the spectrum. $M$–$H$ hysteresis loops were recorded at RT using a SQUID Quantum Design magnetometer.

## 3. Results and discussion

### 3.1. X-Ray diffraction studies

To examine the structural transition in the solid solution, we performed an X-ray diffraction (XRD) study of the $(1 - x)BiFeO_3$-$xBaTi_{0.9}Zr_{0.1}O_3$ system in the range $0 \leq x \leq 0.4$. Fig. 1 illustrates the evolution of X-ray diffraction for all compositions. From this figure, the observed high-intensity peaks confirm the phase purity and good crystalline nature of all the synthesized ceramics, without any detected phase parasites except for a slight impurity ($Bi_{25}FeO_{39}$) in BFO marked with an asterisk (*) in the corresponding figure. We notice from Fig. 2 that both peaks (104) and (110) emerge into a single peak (110), accompanied by the fusion of peaks (006) and (202) into a single peak (111) as the substitution rate increases from $x = 0$ to $x = 0.4$. Similarly, within the range of $65° < 2\theta < 68°$, we observe the disappearance of the peak (208) as $x$ evolves. All these observations indicate a significant transformation in the profile structure from rhombohedral to the cubic with the substitution content. Additionally, Fig. 3 reveals the progressive disappearance of the peak superlattice reflection (113) as $x$ increases. This peak results from antiphase rotation of oxygen octahedra about the [001] axis. All these features confirm that the rhombohedral structure
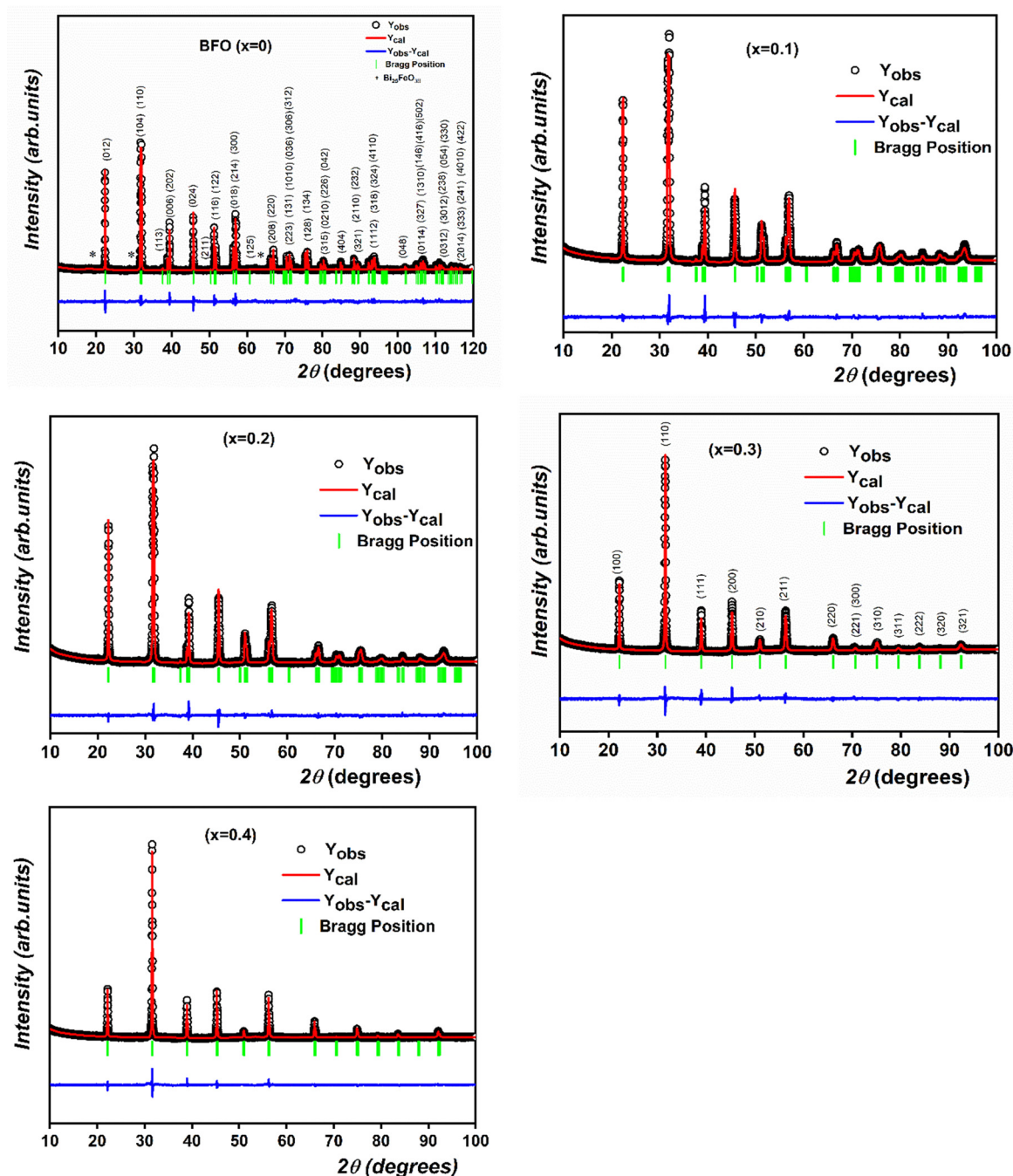
**Fig. 1** The observed, calculated and difference Rietveld's refinement for XRD patterns of $(1 - x)BiFeO_3$-$xBaTi_{0.9}Zr_{0.1}O_3$ system in the range $0 \leq x \leq 0.4$.

with $R3c$ space group is the stable phase of $(1 - x)BiFeO_3$-$xBaTi_{0.9}Zr_{0.1}O_3$ only for $x$ values ranging from 0 to 0.2.

To further analyze the XRD data, Rietveld refinement of the patterns of all prepared compositions was performed using the FullProf program.[23] The observed, calculated and the difference refined XRD patterns of compositions with $x$ = 0, 0.1, 0.2, 0.3 and 0.4 are illustrated in Fig. 1. The results of the Rietveld refinement are summarized in Table 1. All peaks were indexed to the noncentrosymmetric distorted rhombohedral structure with $R3c$ space for compositions $0 \leq x \leq 0.2$, whereas the compositions $0.2 < x \leq 0.4$ are indexed with the

centrosymmetric cubic $Pm\bar{3}m$ space. As illustrative examples, Fig. 1 displays the XRD pattern of BFO indexed to the $R3c$ space group, whereas the pattern for the composition $x$ = 0.3 is indexed to the $Pm\bar{3}m$ space group.

In order to compare the variation of unit cell parameters with compositions ($x$) of the two phases, we have calculated equivalent elementary perovskite cell parameters from the refined hexagonal $c$ and $a$ parameters using the following relationships[24] $a \approx a_H/\sqrt{2}$ and $c \approx c_H/2\sqrt{3}$ for the rhombohedral phase. The evolution of the elementary perovskite cell parameters as a function of compositions ($x$) is shown in
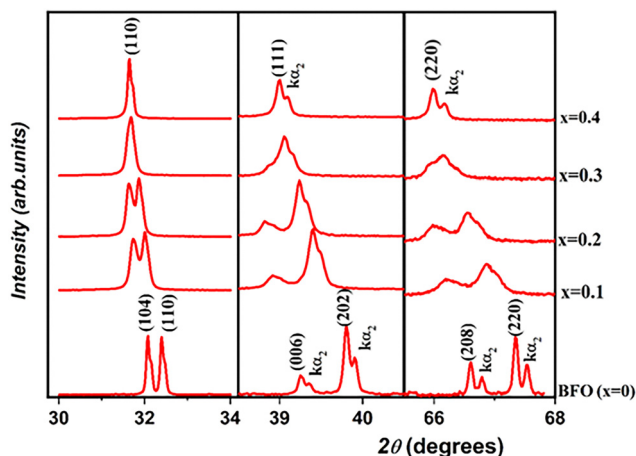
**Fig. 2** Evolution of (104), (110), (006), (202), (208) and (220) peaks as a function of substitution rate ($0 \leq x \leq 0.4$).
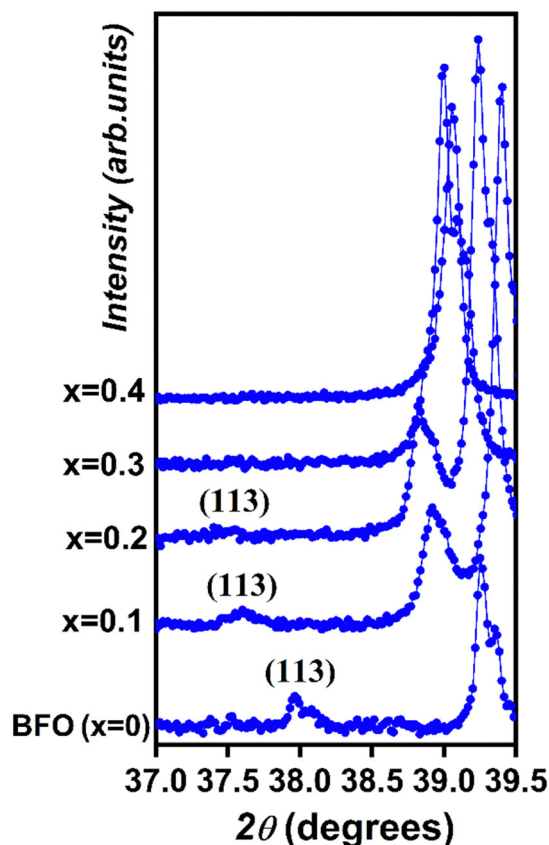


**Fig. 3** Evolution of the superlattice reflection (113) for $x = 0$, 0.1, 0.2, 0.3 and $x = 0.4$.

Fig. 4a and the ratio $c/a$ is depicted in Fig. 4b. From Fig. 4a, a remarkable variation of the parameters with substitution rate ($x$) is observed. This variation is attributed to the disparate ionic radii, either at site A ($Bi^{3+}$ (1.17 Å)/$Ba^{2+}$ (1.42 Å)) or at site B ($Fe^{3+}$ (0.645 Å)/$Ti^{4+}$ (0.605 Å)/$Zr^{4+}$ (0.72 Å)) resulting in lattice distortion. Furthermore, the parameter $c$ shows a clear change up to $x = 0.2$,

revealing the occurrence of a phase transition. On the other hand, from Fig. 4b, the $c/a$ ratio demonstrates a systematic decrease with increasing $x$ until it reaches the value of 1 for compositions with $x = 0.3$ and 0.4, indicating the reduction in lattice distortion from rhombohedral to cubic structure. This distortion necessarily impacts the Wyckoff positions of atoms in the $(1 - x)BiFeO_3$-$(x)BaTi_{0.9}Zr_{0.1}O_3$ system. In our structural study, $Bi^{3+}/Ba^{2+}$ and $Fe^{3+}/Ti^{4+}/Zr^{4+}$ ions are positioned at the 6(a) Wyckoff site while $O^{2-}$ ions reside at the 18(b) sites for compositions with the space group $R3c$. Following the approach outlined by Megaw et al.,[24] the coordinates of all atoms within the asymmetric unit cell of the $R3c$ space group can be expressed as functions of displacement parameters $s$, $t$, $d$, and $e$. These parameters are represented in the Wyckoff positions as: $Bi^{3+}/Ba^{2+}$ (0, 0, 1/4 + s), $Fe^{3+}/Ti^{4+}/Zr^{4+}$ (0, 0, t), and $O^{2-}$ ($1/6 - 2e - 2d$, $1/3 - 4d$, $1/12$). In the cubic phase associated with the $Pm\bar{3}m$ space group, the $Bi^{3+}/Ba^{2+}$ ions are situated at the 1(a) site (0, 0, 0), $Fe^{3+}/Ti^{4+}/Zr^{4+}$ ions occupy the 1(b) site (1/2, 1/2, 1/2), and $O^{2-}$ ions are located at the 3(c) sites (1/2, 1/2, 0). In the event of local disorder within the structure, the cations and anions may also be present at alternative Wyckoff sites. Therefore, the determination of Wyckoff positions allows us to deduce the antiphase rotation (tilt, ($\omega$)) as well as the lattice-scale polarization ($P$).

The configuration of the antiphase rotation (tilt, ($\omega$)) of the adjacent $FeO_6$ oxygen octahedra around the [001] direction is achieved in the $R3c$ space group ($a^-a^-a^-$ in Glazer's notations) as observed in the rhombohedrally distorted perovskite of BFO.[8] However, this configuration is not present in the cubic case with the $Pm\bar{3}m$ space group ($a^0a^0a^0$ in Glazer's notations). In this case, the calculation of $\omega$ is based on the following relation:[24]
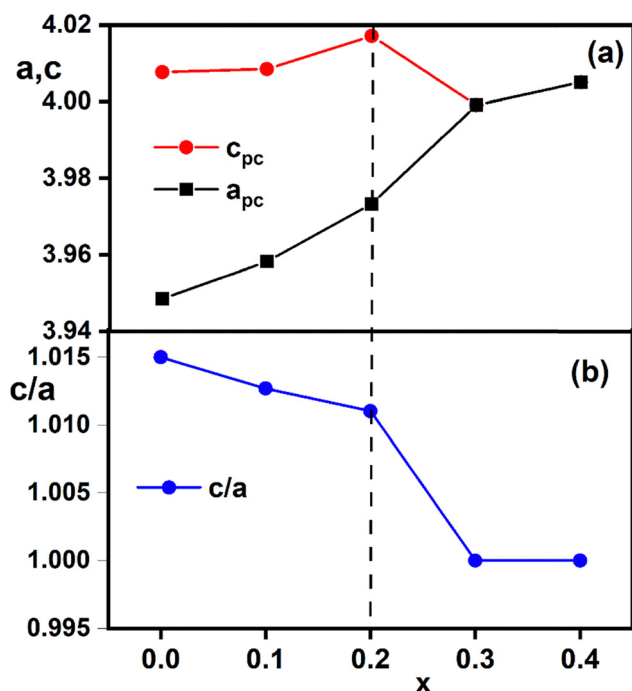
$$\omega = \tan^{-1}\left(4e3^{1/2}\right) \quad (1)$$

The different values of $\omega$ calculated for all prepared compositions are summarized in Table 1. We notice that the substitution of $BaTi_{0.9}Zr_{0.1}O_3$ in the BFO lattice decreases the tilt angle $\omega$, indicating the reduction of the rhombohedral distortion towards the cubic phase. This decrease corresponds to a gradual increase in the Fe–O–Fe bond angle. In this context, the strength of the Dzyaloshinskii–Moriya interaction is linked to the level of the tilt angle.[16] This interaction is responsible for spin canting, resulting in the appearance of weak ferromagnetic. Thus, as the tilt angle decreases, the strength of DM interaction diminishes, reducing the remanent magnetization $M_r$. Additionally, this result has an impact on magnetic ordering, which will be discussed in the later section.

On the other hand, the lattice-scale polarization ($P$) can be calculated from the displacement of both $Fe^{3+}/Ti^{4+}/Zr^{4+}$ (tc) and $Bi^{3+}/Ba^{2+}$ (sc) cations from their centrosymmetric position along the direction [001] for the noncentrosymmetric rhombohedral structure. The polarization is then determined by evaluating the displacement $c(s - t)$.[6] The calculated polarizations are summarized in Table 1. We notice that the calculated polarization is reduced with $BaZr_{0.1}Ti_{0.9}O_3$ substitution until $x = 0.2$. Thus, we can point out the role of the stereochemical activity of the Bi lone electron pair that leads to the ferroelectric order.

**Table 1** Refined structural parameters for the compositions of $(1-x)BiFeO_3$-$xBaZr_{0.1}Ti_{0.9}O_3$ $(0 \leq x \leq 0.4)$ obtained from Rietveld analysis of XRD data

| $x$ | 0 | 0.10 | 0.20 | 0.30 | 0.40 |
|---|---|---|---|---|---|
| | $R3c$ | | | $Pm\bar{3}m$ | |
| Space group | $a = b \neq c$, $\alpha = \beta = 90°$, $\gamma = 120°$ | | | $a = b = c$, $\alpha = \beta = \gamma = 90°$ | |
| $a$ (Å) | 5.58397(5) | 5.59783(12) | 5.61909(12) | 3.99914(14) | 4.00505(9) |
| $c$ (Å) | 13.88305(15) | 13.8859(4) | 13.9156(3) | — | — |
| Bi/Ba ($z$) | 0.2951(8) | 0.2938(5) | 0.2883(4) | 0 | 0 |
| Fe/Ti/Zr ($x = y$) | 0 | 0 | 0 | 0.5 | 0.5 |
| Fe/Ti/Zr ($z$) | 0.0162(9) | 0.0175(5) | 0.0145(5) | 0.5 | 0.5 |
| O ($x$) | 0.233(2) | 0.2267(15) | 0.2173(15) | 0.5 | 0.5 |
| O ($y$) | 0.343(2) | 0.3437(13) | 0.3445(12) | 0.5 | 0.5 |
| O ($z$) | 1/12 | 1/12 | 1/12 | 0 | 0 |
| Fe–O–Fe (deg) | 157.0(7) | 158.2(4) | 161.7(4) | 180 | 180 |
| $\omega$ (deg) | 12.03(57) | 10.758(39) | 8.870(41) | — | — |
| Polarization $P$ ($\mu C\ cm^{-2}$) | 61.72(26) | 55.89(15) | 50.30(14) | — | — |
| $R_{wp}$ (%) | 19.8 | 11.4 | 11.0 | 17.1 | 16.1 |
| $\chi^2$ | 4.78 | 3.85 | 2.81 | 3.78 | 3.13 |



**Fig. 4** (a) Variation in unit cell parameters for compositions $0 \leq x \leq 0.4$. (b) The evolution of ratio ($c/a$) as a function of $x$.



**Fig. 5** SEM micrograph of the surface of $(1-x)BiFeO_3$-$xBaZr_{0.1}Ti_{0.9}O_3$ ceramic for compositions $0.1 \leq x \leq 0.4$.

## 3.2. Microstructural studies

The surface morphology and microstructure of samples $x = 0.1$, $x = 0.2$, $x = 0.3$, and $x = 0.4$ were analyzed using scanning electron microscopy (SEM). The SEM surface micrographs of these samples, as depicted in Fig. 5, show a dense morphology with few voids. Each sample presents distinctive morphologies and boundaries. The histogram representing the grain size distribution is in the inset of each SEM image. The histograms indicate the average grain sizes of around 1.5 µm, 2 µm, 3.5 µm and 1.5 µm for $x = 0.1$, $x = 0.2$, $x = 0.3$ and $x = 0.4$, respectively.

As an example, we illustrate the SEM-energy dispersive spectroscopy (SEM-EDS) elements of samples with $x = 0.1$ and $x = 0.3$ in Fig. 6a and b, respectively. This analysis confirms the presence of all elements across the grains. Here, the presence of carbon in the EDS mapping is due to the carbon paint used to fix the sample onto the microscope holder. The distribution of Zr exhibits the lowest intensity, which is attributed to its low concentration, following the chemical equation. The distributions of Bi, Ba, and Ti appear less intense compared to that of Fe in the EDS maps, indicating the formation of Fe-rich regions. This nonuniform distribution suggests a microscopic segregation, which can be explained by the immiscibility between the $BaTi_{0.9}Zr_{0.1}O_3$ and $BiFeO_3$ phases. In fact, the introduction of multiple elements with considerable differences in electronegativity and chemical valence was also observed in the substituted system $BiFeO_3$–$BaTiO_3$, leading to the development of microscopic segregation.[25–27]

## 3.3. Raman scattering spectra

Raman scattering spectroscopy is a highly effective technique for investigating structural distortions. This technique allows for the examination of distortions within a space group through band shifts, as well as the characterization of distortions
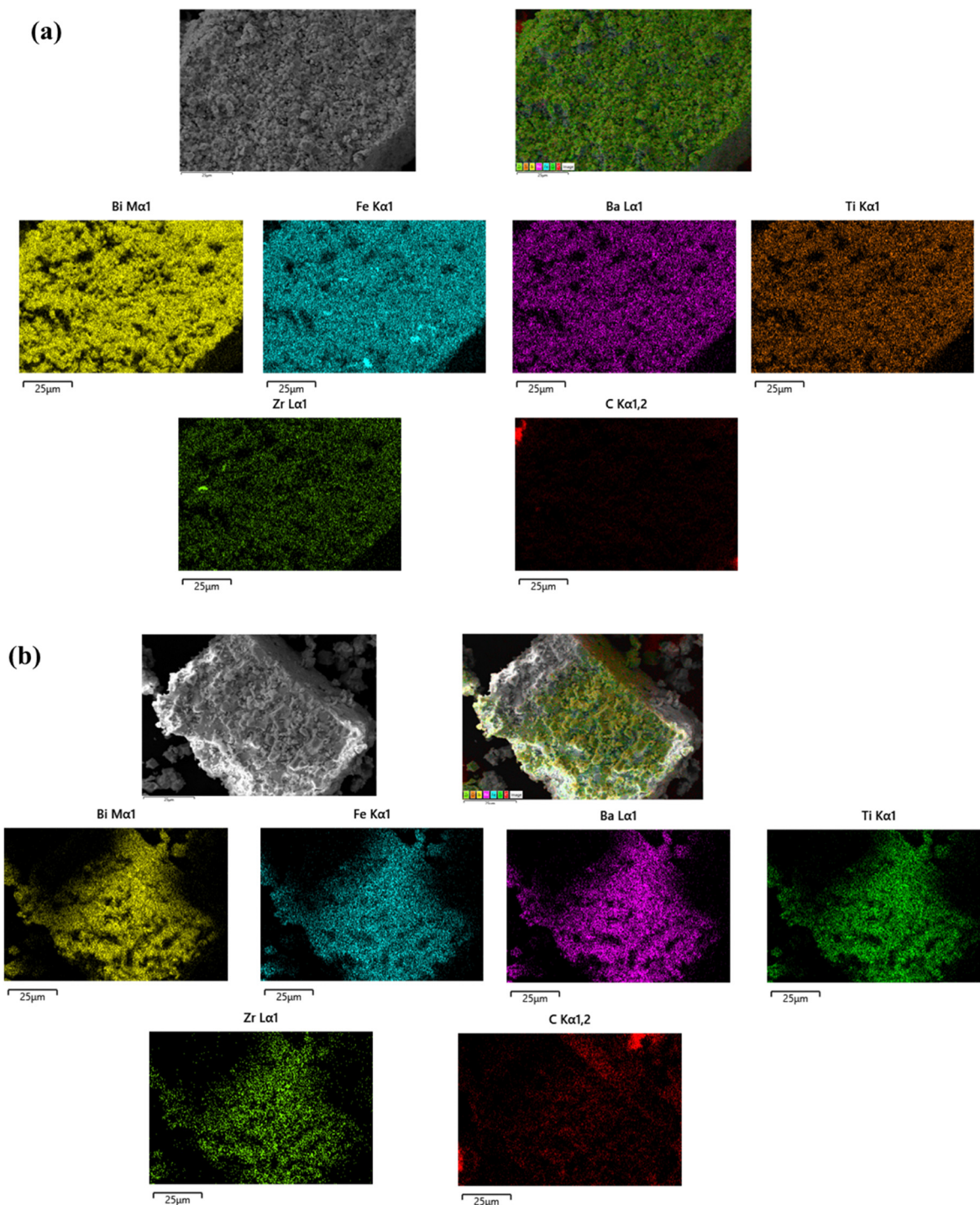
Fig. 6 (a) and (b) SEM−EDS elemental mappings of samples with $x$ = 0.1 and $x$ = 0.3, respectively.

related to a phase transition, involving phenomena such as band splitting and soft modes. At RT, BFO adopts a rhombohedral $R3c$ space group with two formulas in one primitive cell. By comparison to the cubic $Pm\bar{3}m$ structure, the rhombohedral structure can be described by an antiphase tilt of the adjacent $FeO_6$ octahedron and a displacement of both $Fe^{3+}$ and $Bi^{3+}$ cations from their centrosymmetric position along the direction [001]. According to group theory, the 10 atoms in the unit cell of

the rhombohedral $R3c$ ($C_{3v}$) structure lead to 13 Raman phonon modes:[28] $\Gamma_{\text{Raman},R3c} = 4A_1 + 9E$.

Fig. 7 depicts the Raman scattering spectra of the composition $0 \leq x \leq 0.4$ at RT. From this figure, we can see that all Raman modes broaden as $x$ increases. This observation can be attributed to lattice anharmonicity and disorder caused by variations in the occupancy of the Bi and Fe sites. On the other hand, the $A_{1-1}$ mode ($\sim 140$ cm$^{-1}$) is likely dominated by the

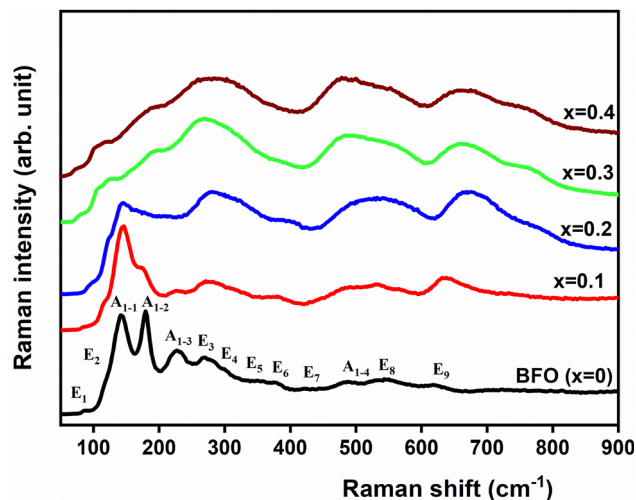**Fig. 7** Raman spectra of all composition of $(1 - x)BiFeO_3$-$xBaZr_{0.1}Ti_{0.9}O_3$ system ($0 \leq x \leq 0.4$) recorded at RT.

Bi–O covalent bond. This bond is responsible for controlling the ferroelectric phase of BFO.[29] In our case, the Raman spectra provide evidence that the $A_{1-1}$ mode decreases in intensity with the substitution rate up to composition $x = 0.2$, which later disappears completely starting from $x = 0.3$. This observation suggests a reduction in the stereochemical activity of the $6s^2$ lone pair electrons associated with $Bi^{3+}$ ions, which occurs due to the substitution of $Bi^{3+}$ by $Ba^{2+}$. This decrease in stereochemical activity impacts the long-range ferroelectric ordering and consequently reduces the ferroelectric characteristics of the system. This trend supports the XRD study, where the polarization deduced from lattice parameters diminishes with the substitution rate $x$. Furthermore, the vibration mode ($A_{1-3}$) detected around 230 $cm^{-1}$ is possibly associated with the tilts of the $FeO_6$ octahedron or $\omega$.[29] The decrease in its intensity with $x$ is consistent with the reduction of the tilt $\omega$ obtained previously through the refinements of XRD pattern refinements. The vanishing of the mode ($A_{1-3}$) observed in the compositions $x = 0.3$ and 0.4 suggests their cubic symmetry.

As previously mentioned in the XRD section, the system $(1 - x)$-$BiFeO_3$-$xBaTi_{0.9}Zr_{0.1}O_3$ transforms into a cubic phase when $x$ exceeds 20%. In the cubic phase, the irreducible representation for the optical phonons is denoted as $\Gamma_{opt} = 3F_{1u} + F_{2u}$. Here, the $F_{1u}$ mode is infrared active, while $F_{2u}$ is considered a "silent mode" as it remains inactive in both Raman and infrared spectroscopy. Therefore, we anticipate the absence of Raman active modes in the cubic phase. However, in the cubic phase for $x = 0.3$ and 0.4, the mode of the rhombohedral structure remains active in the cubic phase, which is caused by the breakdown of the Raman selection rule and substitutional disorder at the cation site. These modes essentially reflect the phonon density of states.[30]

### 3.4. Magnetic properties using Mössbauer spectroscopy and hysteresis loops

To highlight the effect of $Ba(Ti_{0.9}Zr_{0.1})O_3$ substitution on the spin cycloidal structure of BFO and to find the oxidation state

of the Fe ions and their structural environment, we carried out $^{57}Fe$ Mössbauer spectrometry at RT.[5] The obtained Mössbauer spectra for $(1 - x)BiFeO_3$-$xBaZr_{0.1}Ti_{0.9}O_3$, where $0 \leq x \leq 0.4$ are shown in Fig. 8a. Here, the BFO spectrum is shown as a reference in order to emphasize the effects of $Ba(Ti_{0.9}Zr_{0.1})O_3$ substitution. For our prepared pure BFO ceramic ($x = 0$), the spectrum is fitted by the model proposed by D. Lebeugle *et al.*,[5] which links the observed spectral asymmetry to the spiral magnetic structure of $Fe^{3+}$ ions. With this model we obtained the hyperfine parameter values, $H_{hf} = 498$ kOe, $\Delta E_Q = 0.51$ mm $s^{-1}$ and $\delta = 0.40$ mm $s^{-1}$ at RT. These values confirm that Fe is found only as $Fe^{3+}$ in the octahedral environment. They agree with those obtained in ref. 5 from BFO single crystals at the same temperature.

The Fig. 8a shows also symmetrical lines Mössbauer spectra with line-width broadening for samples with $x = 0.1$, 0.2 and 0.3. This may indicate the presence of $Fe^{3+}$ sites distribution in the sample. Indeed, the substitution of BFO with $Ba(Ti_{0.9}Zr_{0.1})O_3$ introduces chemical disorder due to the random replacement of $Fe^{3+}$ ions with $Ti^{4+}$ and $Zr^{4+}$ ions within the BFO structure. This disorder reduces spectral asymmetry and broadens the line widths, making the cycloidal model less effective for fitting the spectra. In response to these changes, we adopted a fitting model based on a discrete distribution of magnetic sextets. In this model, the step size of the hyperfine field distribution and the line width of the sextuplet are fixed, while the isomer shift and quadrupole shift values are fitted but remain common across all sextets.

Fig. 8b shows the obtained hyperfine distribution obtained as a result of the fitting. In order to study the effect of the substitution on the environment of the $Fe^{3+}$ ions, we carried out an analysis with a Poisson distribution. We considered that the value of the area of each sextuplet of the hyperfine field distribution (Fig. 8b) represents the probability $P(X = k)$ that a $Fe^{3+}$ site is surrounded by $k$ nearest $Ti^{4+}$ or $Zr^{4+}$ neighbors, such that:

$$P(X = k) = \frac{\lambda^k}{k!} e^k \qquad (2)$$

where $\lambda$ is the variance of the Poisson distribution.

Mössbauer spectrometry results indicate that the substitution of $Fe^{3+}$ ions with $Ti^{4+}$ and $Zr^{4+}$ induces cationic disorder, which weakens or even suppresses the cycloidal magnetic structure. As shown in Fig. 9, analysis of this disorder using a Poisson distribution reveals an increase in variance from $\lambda = 3.9$ to 5.7 as the substitution level rises from $x = 0.1$ to 0.2. This increase suggests a higher degree of disruption in the cycloidal magnetic structure of $Fe^{3+}$ ions, driven by the Dzyaloshinskii–Moriya (DM) interaction, which becomes subordinate to the exchange interaction. For $x > 0.3$, the cationic distribution broadens further, indicating an escalation in structural disorder, while magnetic interactions between $Fe^{3+}$ ions progressively weaken.

Fig. 10 illustrates the evolution of mean hyperfine parameters as a function of the substitution rate $x$. The mean hyperfine field decreases with increasing $x$, confirming the substitution of $Fe^{3+}$ by non-magnetic $Ti^{4+}$ and $Zr^{4+}$ ions. The
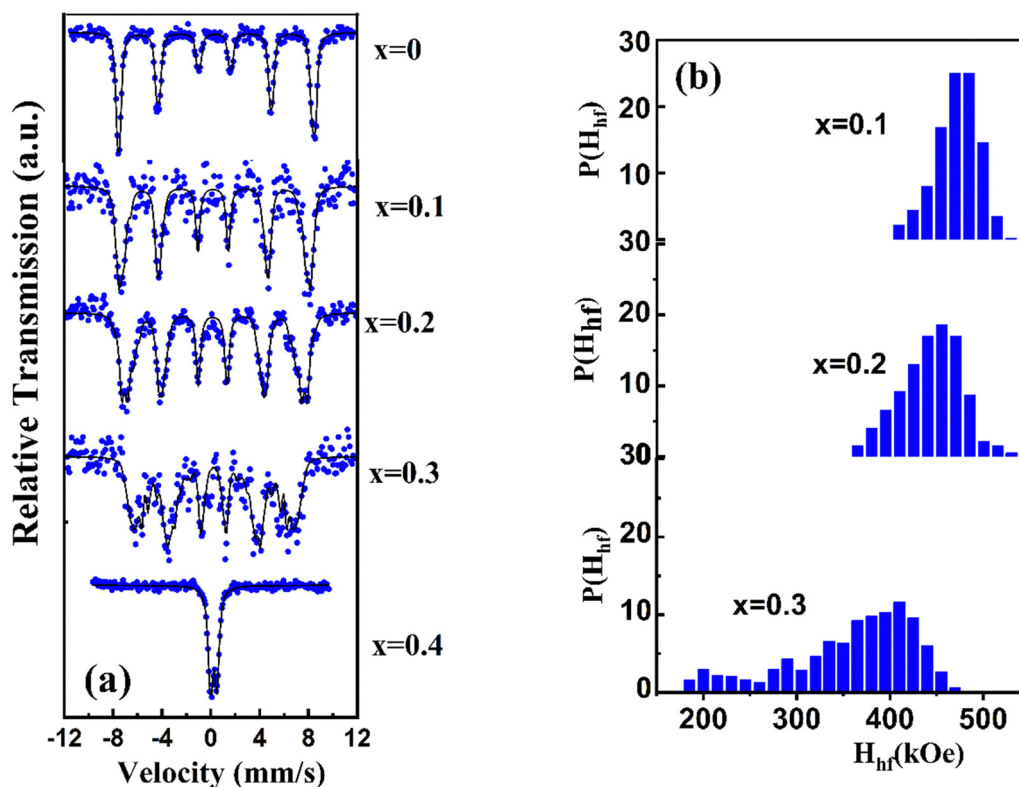
Fig. 8 (a) Mössbauer spectra of $(1-x)BiFeO_3-xBaZr_{0.1}Ti_{0.9}O_3$ system ($0 \leq x \leq 0.4$) recorded at RT (b) hyperfine field distribution.
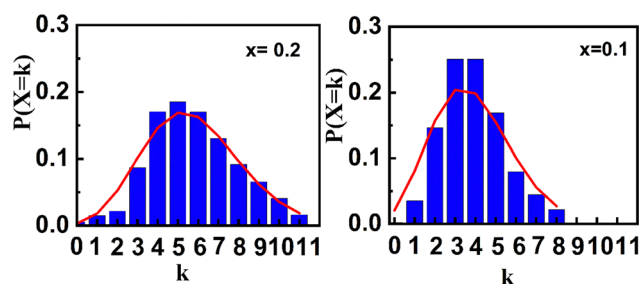


Fig. 9 Plots of the Poisson distribution expressing the probability that a $Fe^{3+}$ site is surrounded by $k$ nearest neighbors in $Ti^{4+}$ and $Zr^{4+}$ for both compositions, $x = 0.1$ and $x = 0.2$. The blue bars represent the frequency histogram and the red curve corresponds to the Poisson distribution.

nearly constant isomer shift indicates that the valence state of Fe remains unchanged upon substitution.

The quadrupole splitting/shift ($\Delta E_Q/2\varepsilon$) arises from the interaction between the nuclear quadrupole moment (eQ) and the electric field gradient ($\nabla \vec{E}$) at the nucleus, providing insight into the local symmetry of the Mössbauer absorber, in this case, $^{57}Fe$ nuclei. A low $\Delta E_Q$ value, close to zero, typically corresponds to a highly symmetric environment. The observed decrease in $\Delta E_Q/2\varepsilon$ for $x \neq 0$ suggests a significant modification in the local symmetry, indicating a transition toward higher-symmetry environment around $Fe^{3+}$ due to substitution. This result confirms the structural transition from the $R3c$ rhombohedral to $Pm\bar{3}m$ cubic observed by XRD and Raman spectroscopy with increasing substitution rate.
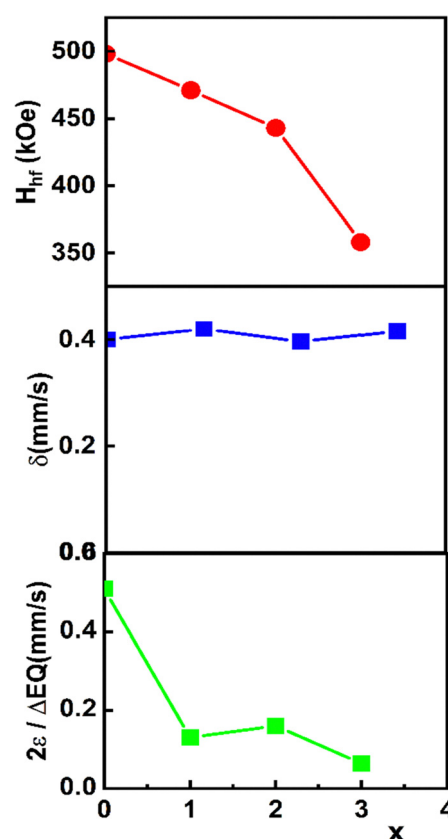


Fig. 10 Substitution rate dependence of mean hyperfine parameters values. $H_{hf}$: hyperfine field, $\delta$: isomer shift, $\Delta E_Q/2\varepsilon$: quadrupole splitting/shift.

At $x$ = 0.4, the Mössbauer spectrum exhibits paramagnetic behavior, with a Néel temperature below 300 K.[19] The obtained hyperfine parameter values are, $\delta$ = 0.38 mm s$^{-1}$ and $\Delta E_Q$ = 0.47 mm s$^{-1}$ at RT.

Fig. 11 depicts the $M$–$H$ cycles for $(1 - x)$BiFeO$_3$-$x$Ba-Ti$_{0.9}$Zr$_{0.1}$O$_3$ ceramics with $x$ ranging from 0 to 0.4 at 300 K and 2 K. Various parameters such as $M_s$ at 60 kOe, $M_r$, and $H_c$ are extracted from these cycles and tabulated in Table 2 at 300 K and 2 K. In the pure BFO, the observation of a low value of remanent magnetization is due to the presence of a small

quantity of Bi$_{25}$FeO$_{39}$ detected in XRD analysis.[5] This finding is consistent with the results reported in the work of Saha et al.[31] From Fig. 11, the value of $M_r$ for $x$ = 0.1 and $x$ = 0.2 shows an improvement in the magnetic order compared to BFO due to the suppression of spin cycloid structure, as investigated by Mössbauer spectroscopy. Furthermore, Mössbauer data show no evidence of Fe$^{2+}$, ruling out the possibility that the increase in $M_r$ for $x$ = 0.1 and $x$ = 0.2 is due to the presence of Fe$^{2+}$.[32]

As mentioned in section XRD, the same trend for $M_r$ and the tilt angle $\omega$ is expected. According to the XRD studies, the tilt
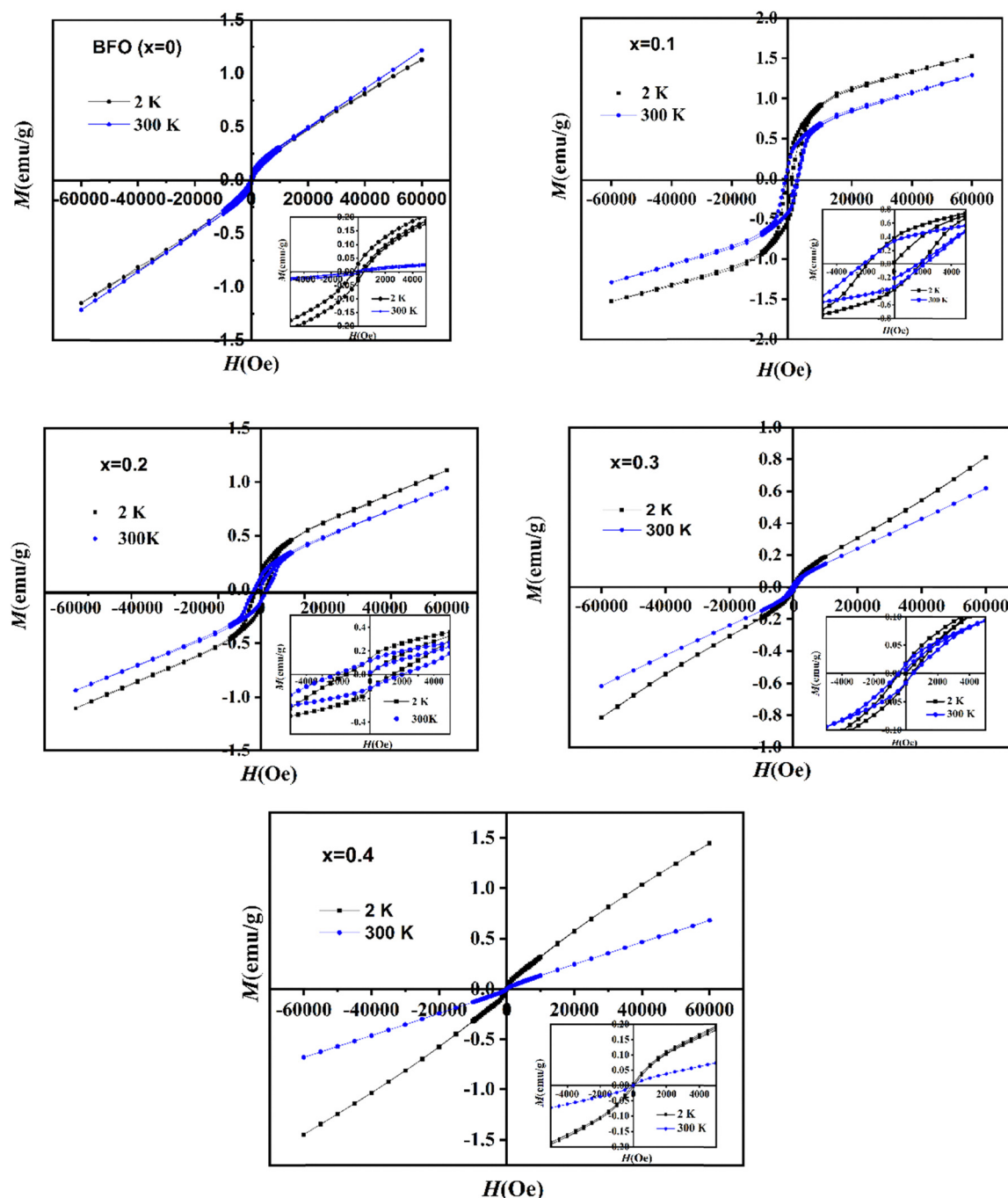


**Fig. 11** Field ($H$) dependence of magnetization ($M$) of $(1 - x)$BiFeO$_3$-$x$BaZr$_{0.1}$Ti$_{0.9}$O$_3$ system ($0 \leq x \leq 0.4$) measured at 2 and 300 K.

**Table 2** $M_s$, $M_r$ and $H_c$ deduced from $M–H$ response for 2 and 300 K

| | $M_s$ (emu g$^{-1}$) at 60 kOe | | $M_r$ (emu g$^{-1}$) | | $H_c$ (Oe) | |
|---|---|---|---|---|---|---|
| $x$ | 300 K | 2 K | 300 K | 2 K | 300 K | 2 K |
| 0 | 1.01 | 1.12 | 0.026 | 0.029 | 335 | 390 |
| 0.1 | 1.28 | 1.52 | 0.34 | 0.38 | 2120 | 1850 |
| 0.2 | 0.9 | 1.1 | 0.11 | 0.22 | 2000 | 1500 |
| 0.3 | 0.61 | 0.81 | 0.016 | 0.017 | 450 | 415 |
| 0.4 | 0.68 | 1.44 | 0 | 0.004 | 0 | 60 |

angle exhibits a systematic decrease with increasing substitution $x$. However, $M_r$ reaches a maximum at the composition $x = 0.1$ both at 2 K and 300 K (Fig. 12a). The nonmonotonic dependence of $M_r$ with the tilt angle $\omega$ was detected. The substitution of $Fe^{3+}$ by nonmagnetic $Zr^{4+}/Ti^{4+}$ reduces the amount of the interaction DM in the composition $x = 0.1$, as obtained in the Mössbauer spectroscopy studies. This feature allows the activation of the weak ferromagnetism set in BFO. In fact, we can explain the appearance of the weak ferromagnetism similarly to the system $(1 − x)BiFeO_3$-$xPbTiO_3$, which is due to the broken cycloid spin structure (as schematized in Fig. 7 of the work of V. F. Freitas *et al.*[33]). Thus, we can suggest the complete destruction of the spin cycloid at $x = 0.1$ which explains the highest value of $M_r$ for $x = 0.1$. After the complete suppression of the cycloid, the reduction in $M_r$ for $x > 0.10$, is attributed to the decrease of the tilt angle. According to Mössbauer spectroscopy investigation, the interaction DM is significantly weakening and yields to the exchange interaction in the G-type antiferromagnetic order of $Fe^{3+}$ ions within the BFO structure. For the composition $x = 0.3$, the magnetic interactions between $Fe^{3+}$ ions progressively weaken, and the remanent magnetization $M_r$ approaches zero (as shown in Fig. 12a). For higher doping, *i.e.*, for $x = 0.4$, $M_r$ completely vanishes, suggesting a paramagnetic phase, consistent with the results observed in the Mössbauer studies.

In Fig. 12b, the value of the coercive field $H_c$ at 300 K is higher than 2 K, respectively, for the compositions $x = 0.1$ and 0.2. This result suggests the existence of magnetoelectric coupling in the compositions $x = 0.1$ and $x = 0.2$. Indeed, according to the work of Park *et al.*,[19] the presence of magnetoelectric coupling in the $(1 − x)BiFeO_3$-$xBaTiO_3$ solid solution nanostructures could potentially explain the decrease in coercivity at low temperatures compared to the value at RT. Referring to the expression of $H_c$ given by the following equation:[34]

$$H_c = \frac{2k_u}{M_s} \quad (3)$$

where $M_s$ is the saturation magnetization and $k_u$ is the uniaxial magnetic anisotropy, they demonstrate that the magnetoelectric coupling contributes to the reduction of $k_u$ leading to the decrease of the coercive field $H_c$. The uniaxial magnetic anisotropy energy is modified in the presence of magnetoelectric coupling in accordance with eqn (4):

$$k'_u = k_u - \chi_\perp \frac{(\beta P_Z)^2}{2} \quad (4)$$

where, $k'_u$ denotes effective uniaxial magnetic anisotropy, $\beta$ represents the magnetoelectric coefficient associated with the Dzyaloshinsky–Moriya magnetic field, $P_Z$ is the spontaneous polarization, and $\chi_\perp$ indicates the magnetic susceptibility in the direction perpendicular to the antiferromagnetic vector.[13,17] In the same figure, according to the work of K. Chakrabarti *et al.*,[35] we can attribute the origin of the highest value of the coercive field $H_c$ for the composition $x = 0.1$ at 2 K and 300 K to significant magnetoelastic and magnetocrystalline anisotropy. The highest values of $M_s$ and $M_r$ are also observed at $x = 0.1$ in the $(1 − x)BiFeO_3$-$(x)BaTi_{0.9}Zr_{0.1}O_3$ system. The comparison of these changes with the system $(1 − x)BiFeO_3$-$xBaTiO_3$[19] is interesting, where the highest values of $M_s$ and $M_r$ match the lowest values of $H_c$ at $x = 0.2$. This difference can be attributed to the effect of Zr since the ionic radius of $Zr^{4+}$ (0.72 Å) is larger than that of $Ti^{4+}$ (0.605 Å). This introduces local structural distortions and strain within the lattice, enhancing the magnetocrystalline anisotropy. In Fig. 12b, the substantial decrease in coercive field $H_c$ at $x = 0.3$ and $x = 0.4$ is due to the change of magnetocrystalline anisotropy, as the rhombohedral structure
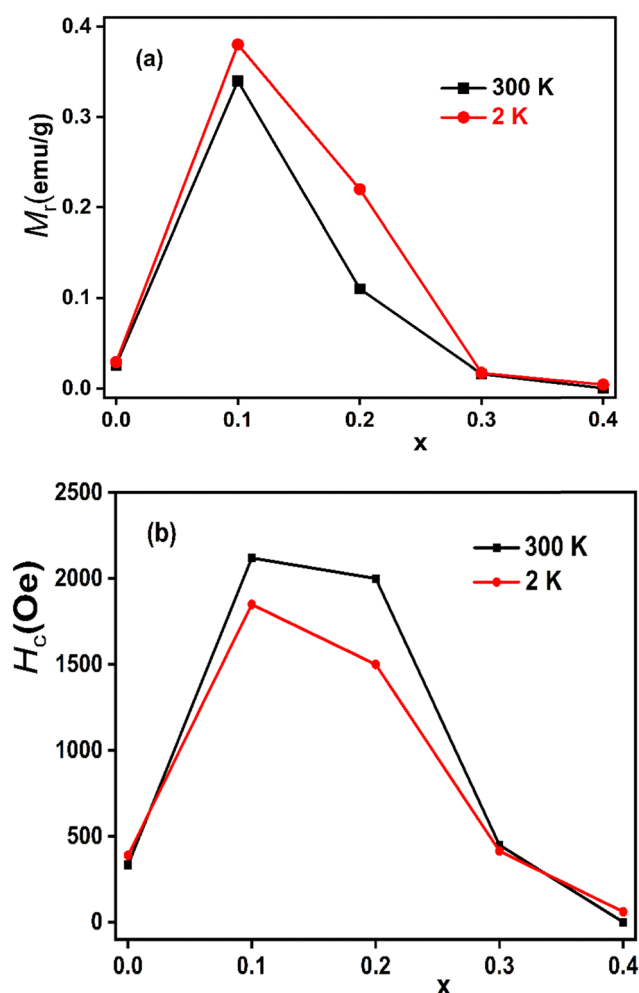


**Fig. 12** (a) Variation of remnant magnetization ($M_r$) (b) the evolution of the coercive field ($H_c$) as a function of $x$ at 2 and 300 K.

emerges toward a highly symmetric cubic phase. This result agrees with the Mössbauer spectroscopy analysis.

## 4. Conclusion

Ceramics from the system $(1 - x)BiFeO_3-(x)BaTi_{0.9}Zr_{0.1}O_3$ with $x = 0-0.4$ were prepared using a conventional solid-state sintering procedure. We thoroughly investigated the crystalline structure and the magnetic properties using XRD, Raman scattering spectroscopy, Mössbauer spectroscopy analysis reveals that the substitution of $Fe^{3+}$ ions with $Ti^{4+}$ and $Zr^{4+}$ induces cationic disorder, which weakens the Dzyaloshinskii–Moriya (DM) interaction. Consequently, the DM interaction becomes subordinate to the exchange interaction in the G-type antiferromagnetic order of $Fe^{3+}$ ions within the BFO structure. This modification may lead to the suppression of the cycloidal spin structure of $Fe^{3+}$ ions in samples with $x = 0.1, 0.2$ and $0.3$. The same analysis indicates a paramagnetic state of composition $x = 0.4$. On the other hand, the magnetic coercivity $(H_c)$ of the compositions $x = 0.1$ and $0.2$ decreases at low temperatures compared to RT. The reason for this effect is related to the magnetoelectric coupling. From Rietveld refinement data, it was demonstrated that the tilt angle $(\omega)$ decreases with the substitution rate in the rhombohedral phase and becomes zero in the cubic phase. This decrease results in a reduction of magnetic properties deduced from the $M–H$ response, except for the composition with $x = 0.1$, which shows an enhancement compared to BFO. Hence, this composition provides a significant remnant magnetization $(M_r)$ equal to $0.34$ emu g$^{-1}$. As a result, substituted BFO could potentially be suitable for the development of several devices, particularly in the field of data storage.

## Author contributions

All authors contributed to the present manuscript. Material synthesis, data collection, and analysis were carried out by Imen Kallel, Zied Abdelkafi, Najmeddine Abdelmoula, Hamadi Khemakhem and Nirina Randrianantoandro. Futhermore, El-Kebir Hlil contributed to the interpretation of the Magnetic properties section. The initial draft of the manuscript was prepared by Imen Kallel in collaboration with Zied Abdelkafi, and all other authors provided comments on previous versions of the manuscript. All authors read and approved the final draft of the manuscript.

## Conflicts of interest

There are no conflicts to declare.

## Data availability

The data available in the article are true and valid, as recognized by the authors. The data that support the findings of this study are available from all authors upon reasonable request.

## Acknowledgements

## References

1  R. Montecillo, C.-S. Chen, Y.-T. Lee, P.-Y. Chen and C.-S. Tu, *J. Eur. Ceram. Soc.*, 2023, **43**, 1941–1951.

2  A. Raza Khan, G. M. Mustafa, S. Kumail Abbas, S. Atiq, M. Saleem, S. M. Ramay and S. Naseem, *Results Phys.*, 2020, **16**, 102956.

3  H. Sun, Z. Luo, C. Liu, C. Ma, Z. Wang, Y. Yin and X. Li, *J. Materiomics*, 2022, **8**, 144–149.

4  G. Catalan and J. F. Scott, *Adv. Mater.*, 2009, **21**, 2463–2485.

5  D. Lebeugle, D. Colson, A. Forget, M. Viret, P. Bonville, J. F. Marucco and S. Fusil, *Phys. Rev. B:Condens. Matter Mater. Phys.*, 2007, **76**, 024116.

6  S. M. Selbach, T. Tybell, M.-A. Einarsrud and T. Grande, *Adv. Mater.*, 2008, **20**, 3692–3696.

7  S. Lee, M. T. Fernandez-Diaz, H. Kimura, Y. Noda, D. T. Adroja, S. Lee, J. Park, V. Kiryukhin, S. W. Cheong, M. Mostovoy and J.-G. Park, *Phys. Rev. B:Condens. Matter Mater. Phys.*, 2013, **88**, 060103.

8  A. Glazer, *Acta Crystallogr., Sect. B*, 1972, **28**, 3384–3392.

9  I. Sosnowska, T. P. Neumaier and E. Steichele, *J. Phys. C-Solid State Phys.*, 1982, **15**, 4835.

10  A. M. Kadomtseva, A. K. Zvezdin, Y. F. Popov, A. P. Pyatakov and G. P. Vorob'ev, *J. Exp. Theor. Phys. Lett.*, 2004, **79**, 571–581.

11  I. Sosnowska and A. K. Zvezdin, *J. Magn. Magn. Mater.*, 1995, **140–144**, 167–168.

12  C. Ederer and N. A. Spaldin, *Phys. Rev. B:Condens. Matter Mater. Phys.*, 2005, **71**, 060401.

13  N. Wang, J. Cheng, A. Pyatakov, A. K. Zvezdin, J. F. Li, L. E. Cross and D. Viehland, *Phys. Rev. B:Condens. Matter Mater. Phys.*, 2005, **72**, 104434.

14  J.-H. Lee, H. J. Choi, D. Lee, M. G. Kim, C. W. Bark, S. Ryu, M.-A. Oak and H. M. Jang, *Phys. Rev. B:Condens. Matter Mater. Phys.*, 2010, **82**, 045113.

15  A. Singh, A. Gupta and R. Chatterjee, *Appl. Phys. Lett.*, 2008, **93**, 022902.

16  A. Singh, A. Senyshyn, H. Fuess, S. J. Kennedy and D. Pandey, *Phys. Rev. B:Condens. Matter Mater. Phys.*, 2014, **89**, 024108.

17  B. Ruette, S. Zvyagin, A. P. Pyatakov, A. Bush, J. F. Li, V. I. Belotelov, A. K. Zvezdin and D. Viehland, *Phys. Rev. B:Condens. Matter Mater. Phys.*, 2004, **69**, 064114.

18  F. Bai, J. Wang, M. Wuttig, J. Li, N. Wang, A. P. Pyatakov, A. K. Zvezdin, L. E. Cross and D. Viehland, *Appl. Phys. Lett.*, 2005, **86**, 032511.

19 T.-J. Park, G. C. Papaefthymiou, A. J. Viescas, Y. Lee, H. Zhou and S. S. Wong, *Phys. Rev. B:Condens. Matter Mater. Phys.*, 2010, **82**, 024431.

20 I. Kallel, H. Khemakhem, Z. Sassi, N. Abdelmoula, E.-K. Hlil and N. Randrianantoandro, *J. Phys. D: Appl. Phys.*, 2022, **55**, 065303.

21 G. D. Achenbach, W. J. James and R. Gerson, *J. Am. Ceram. Soc.*, 1967, **50**, 437.

22 J. Teillet and T. Varret, unpublished Mosfit program (Université du Maine, France, 1984).

23 J. Rodríguez-Carvajal, *FULLPROF,version 2015, Laboratoire Leon Brillouin, CEA-CNRS, France*, https://www.ill.eu/sites/fullprof.

24 H. D. Megaw and C. N. W. Darlington, *Acta Crystallogr., Sect. A*, 1975, **31**, 161–173.

25 D. Wang, Z. Fan, W. Li, D. Zhou, A. Feteira, G. Wang, S. Murakami, S. Sun, Q. Zhao, X. Tan and I. M. Reaney, *ACS Appl. Energy Mater.*, 2018, **1**, 4403–4412.

26 H. Li, J. Zhao, Y. Li, L. Chen, X. Chen, H. Qin, H. Zhou, P. Li, J. Guo and D. Wang, *ACS Appl. Mater. Interfaces*, 2024, **16**, 9078–9087.

27 Z. Yang, Y. Li, B. Wang, J. Pan, A. K. Kleppe and D. A. Hall, *J. Materiomics*, 2024, **10**, 57–69.

28 R. Haumont, J. Kreisel and P. Bouvier, *Phase Transitions*, 2006, **79**, 1043–1064.

29 P. Hermet, M. Goffinet, J. Kreisel and P. Ghosez, *Phys. Rev. B:Condens. Matter Mater. Phys.*, 2007, **75**, 220102.

30 K. K. Mishra, V. Sivasubramanian, R. M. Sarguna, T. R. Ravindran and A. K. Arora, *J. Solid State Chem.*, 2011, **184**, 2381–2386.

31 S. Saha, K. L. Routray, T. K. Nayak and B. Dash, *Braz. J. Phys.*, 2024, **54**, 147.

32 M. Shu, D. Wang, S. Li, B. Yang, L. Yin, W. Song, J. Yang, X. Zhu and Y. Sun, *J. Appl. Phys.*, 2020, **128**, 164101.

33 V. F. Freitas, T. G. M. Bonadio, G. S. Dias, O. A. Protzek, A. N. Medina, L. F. Cótica, I. A. Santos, D. Garcia and J. A. Eiras, *J. Appl. Phys.*, 2013, **113**, 114105.

34 A. H. Morrish, IEEE Press, Piscataway, 2001.

35 K. Chakrabarti, K. Das, B. Sarkar and S. K. De, *J. Appl. Phys.*, 2011, **110**, 103905.